Supporting information

Gas Diffusion Governs the Intracellular Dissolution of Lipid-Shelled Microbubbles

Yann Ferry[1], Andrei Hancu[1], Andrew Kristof[2], Pavlos Anastasiadis[3,4,5,6], John Blazeck[2,7,8,9,10], Costas Arvanitis[1,11,§]

[1]Coulter Department of Biomedical Engineering, Georgia Institute of Technology and Emory University, Atlanta, Georgia, USA

[2]School of Chemical and Biomolecular Engineering, Georgia Institute of Technology, Atlanta, GA

[3]Department of Neurosurgery, University of Maryland School of Medicine, Baltimore, MD

[4]Department of Diagnostic Radiology and Nuclear Medicine, University of Maryland School of Medicine, Baltimore, MD

[5]Fischell Department of Bioengineering, University of Maryland, College Park, MD

[6]Brain Tumor Program, University of Maryland Marlene and Stewart Greenebaum Comprehensive Cancer Center, Baltimore, MD

[7]Parker H. Petit Institute of Bioengineering and Bioscience, Georgia Institute of Technology, Atlanta, GA, USA

[8]Integrated Cancer Research Center, Georgia Institute of Technology, Atlanta, GA, USA

[9]Georgia Immunoengineering Consortium, Emory University and Georgia Institute of Technology, Atlanta, GA, USA

[10]Winship Cancer Institute, Emory University, Atlanta, GA, USA

[11]Woodruff School of Mechanical Engineering, Georgia Institute of Technology, Atlanta, Georgia, United States

§ Corresponding author

Video S1 - 3D B-Mode and AMPI (reconstruction) imaging of MB-Mac leakage from injection site (https://youtu.be/BucENR-dEF8)

Video S2 - B-Mode and AMPI imaging of MB-Mac backflow along the needle track (https://youtu.be/PkF7f8ArvIA)

Video S3 - B-Mode and AMPI imaging of MB-Mac leakage into peritumoral tissue during injection (https://youtu.be/zsWB4JoG7-s)

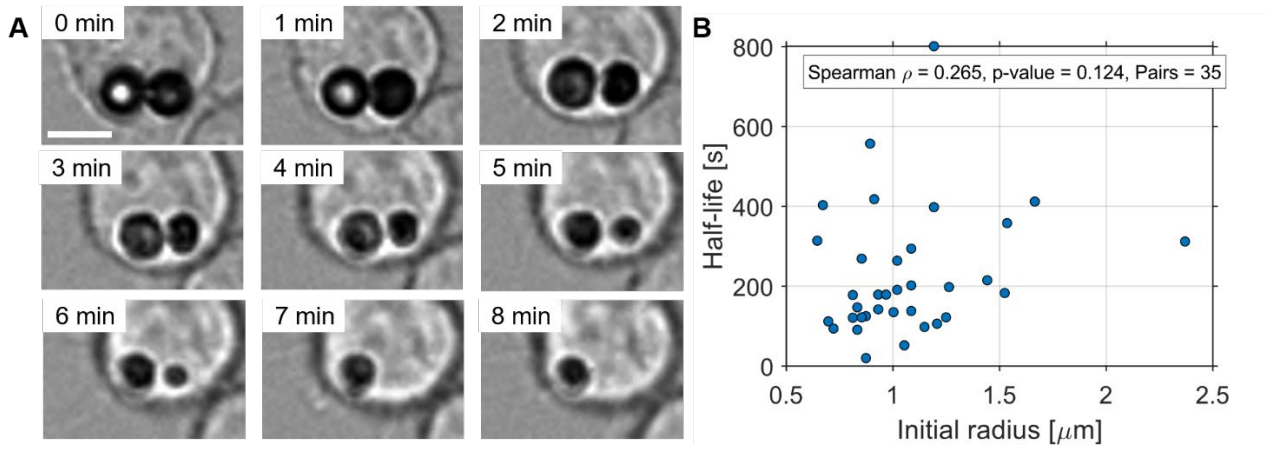


Figure S1. Internalized MBs exhibit heterogeneous shell properties at a similar initial radius. **(A)** Live cell microscopy imaging of two intracellular MBs with similar initial radius but different shrinking dynamics (Scale bar = 5 μm). **(B)** Correlation between initial MB radius and half-life. Each point represents a single microbubble. Spearman's rank correlation coefficient was ρ = 0.265 (N = 35, p = 0.124).

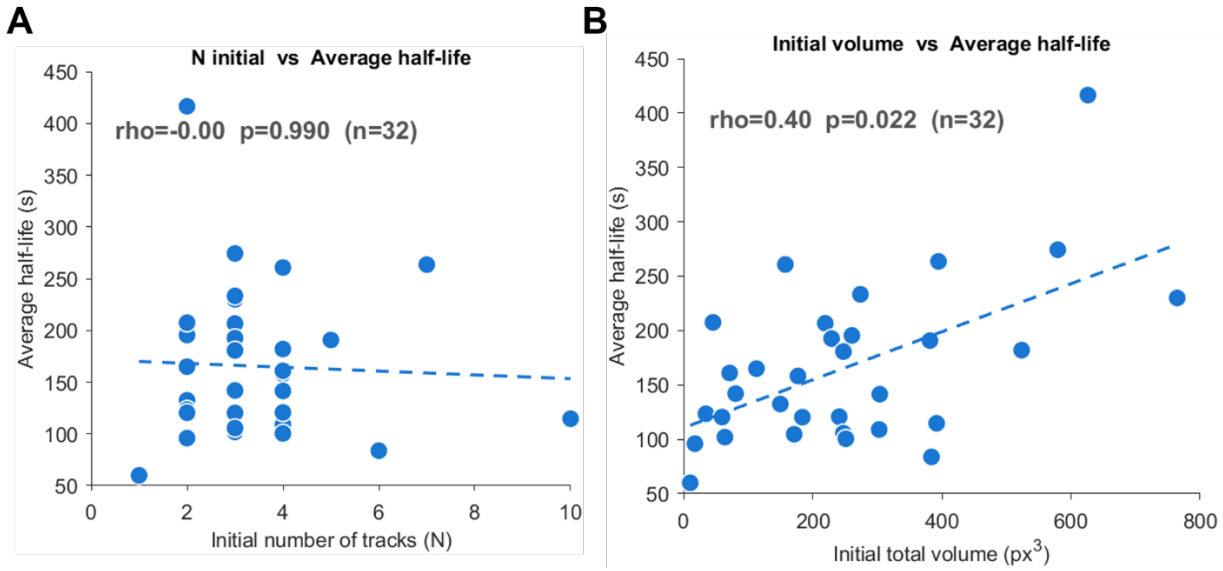
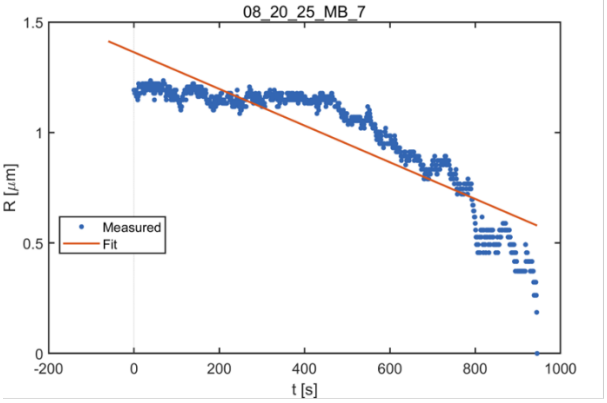
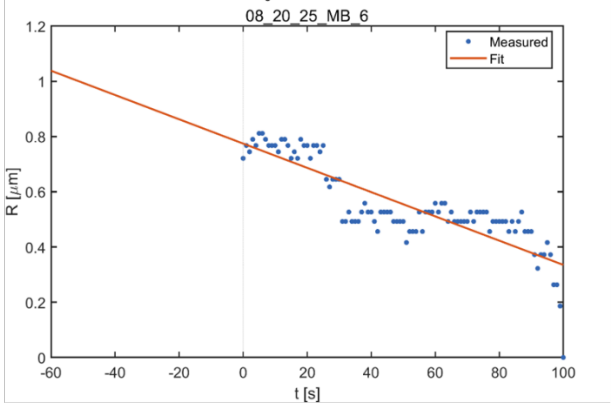


Figure S2. Correlation analysis between microbubble population and their average half life at the cellular level. **(A)** Correlation analysis between initial number of MB in a cell and their average half-life. Each point represents a single cell. Spearman's rank correlation coefficient was ρ = 0.00 (N = 32, p = 0.990). **(B)** Correlation analysis between initial total volume of MBs in a cell and their average half-life. Each point represents a single cell. Spearman's rank correlation coefficient was ρ = 0.4 (N = 32, p = 0.022).

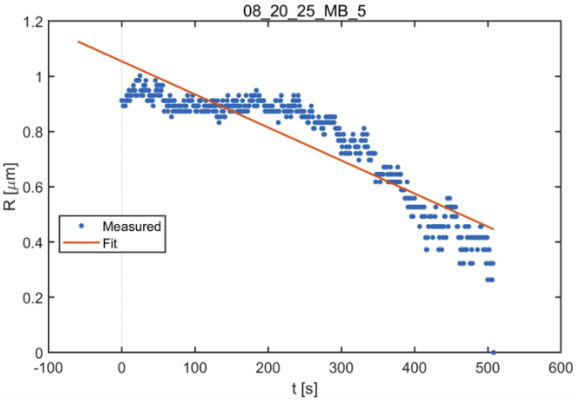
Least Squares Fit | h = 1.06 μm/s, R_0 = 0.854 μm | RMSE = 0.117 μm, R^2 = 0.7907



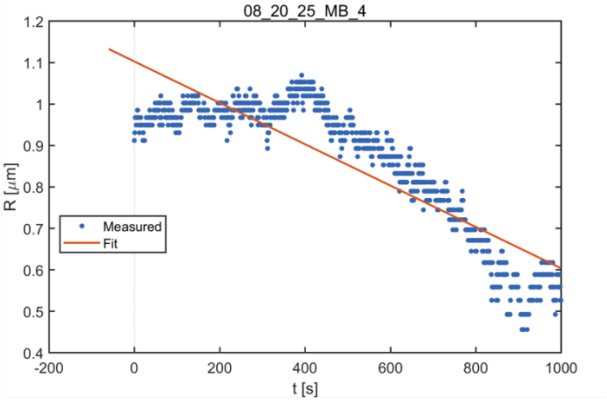
Least Squares Fit | h = 5.63 μm/s, R_0 = 0.672 μm | RMSE = 0.0768 μm, R^2 = 0.7355



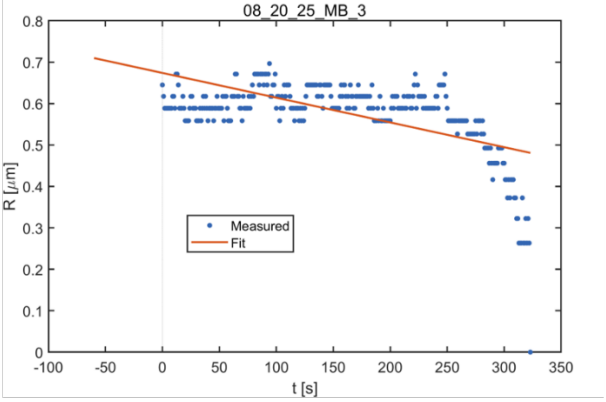
Least Squares Fit | h = 1.53 μm/s, R_0 = 0.718 μm | RMSE = 0.0832 μm, R^2 = 0.8172



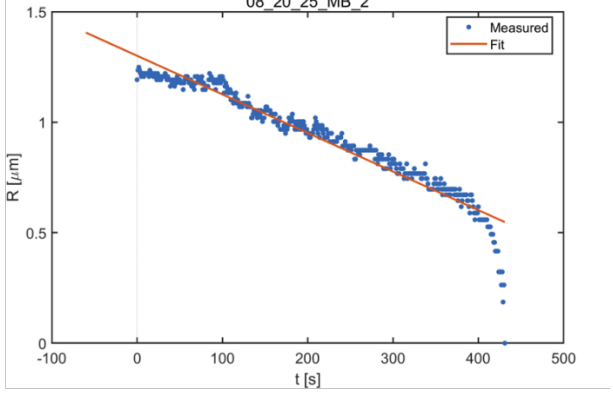
Least Squares Fit | h = 0.64 μm/s, R_0 = 0.721 μm | RMSE = 0.0797 μm, R^2 = 0.7661



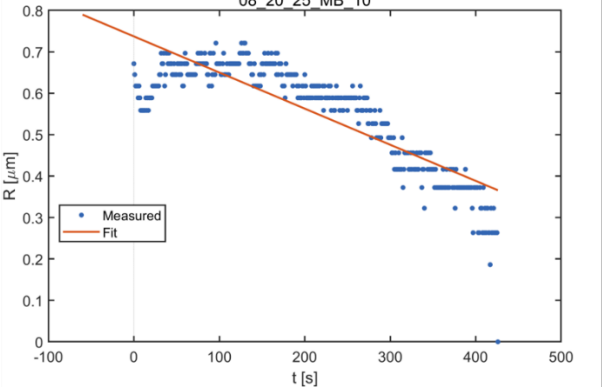
Least Squares Fit | h = 0.766 μm/s, R_0 = 0.5 μm | RMSE = 0.0708 μm, R^2 = 0.3176



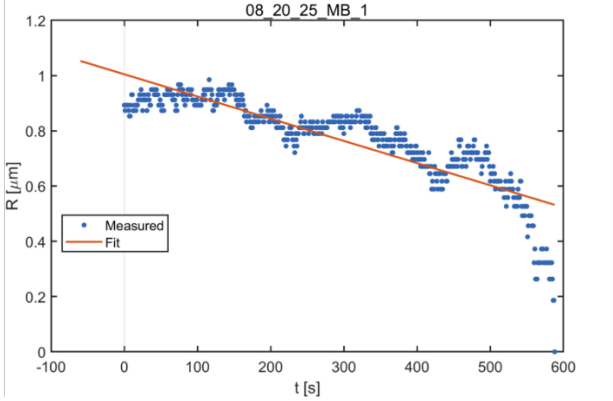
Least Squares Fit | h = 2.24 μm/s, R_0 = 0.849 μm | RMSE = 0.0592 μm, R^2 = 0.9312



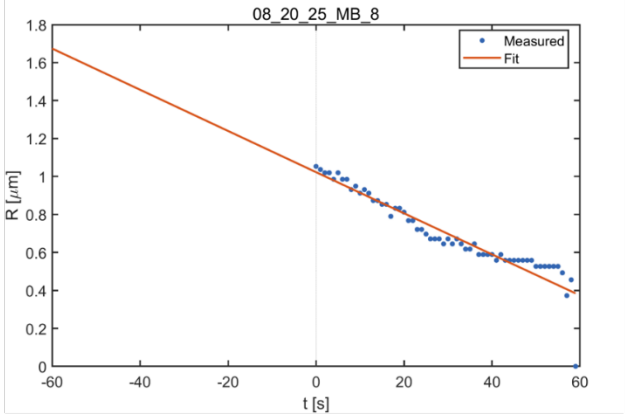
Least Squares Fit | h = 1.12 μm/s, R_0 = 0.544 μm | RMSE = 0.064 μm, R^2 = 0.7381



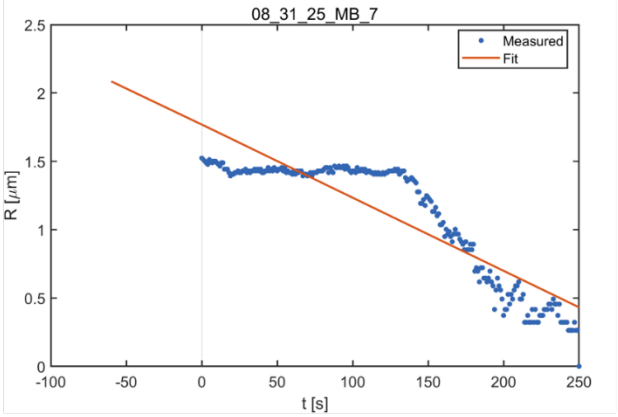
Least Squares Fit | h = 1.03 μm/s, R_0 = 0.682 μm | RMSE = 0.0803 μm, R^2 = 0.7435



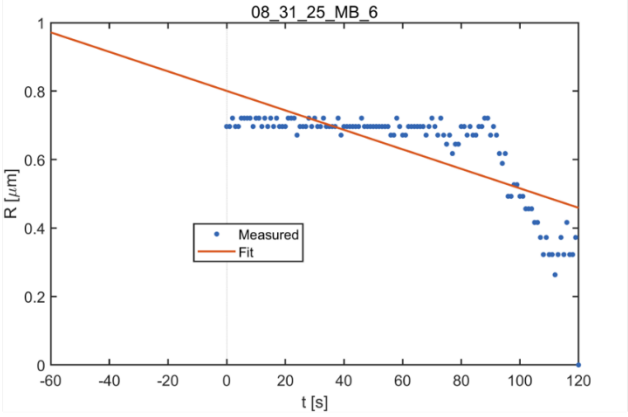
Least Squares Fit | h = 13.8 μm/s, R_0 = 0.954 μm | RMSE = 0.064 μm, R^2 = 0.8954



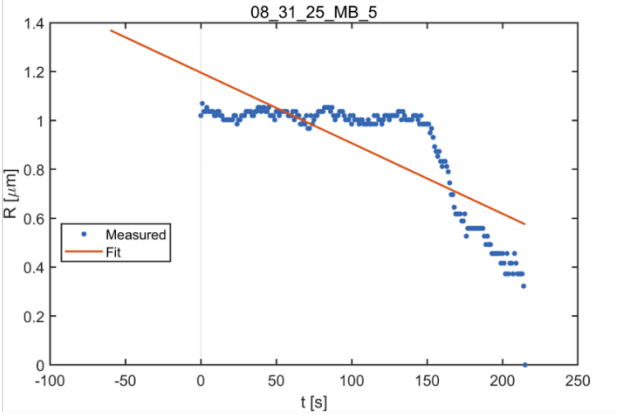
Least Squares Fit | h = 6.84 μm/s, R_0 = 1.13 μm | RMSE = 0.195 μm, R^2 = 0.7981



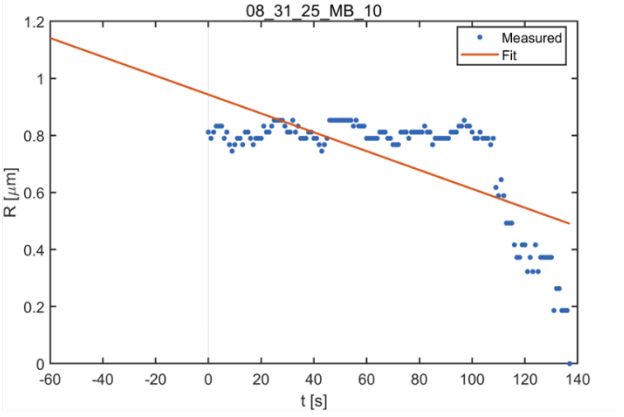
Least Squares Fit | h = 3.65 μm/s, R_0 = 0.639 μm | RMSE = 0.0923 μm, R^2 = 0.5372



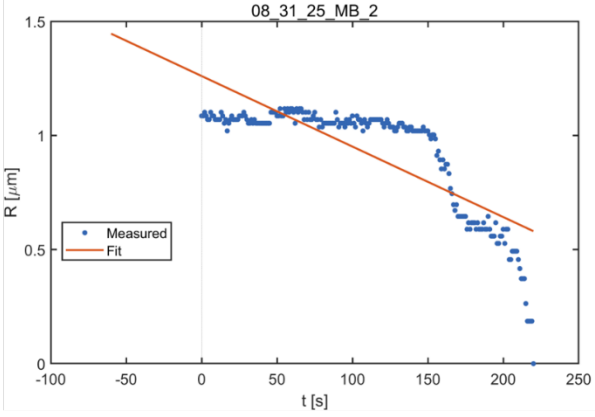
Least Squares Fit | h = 3.7 μm/s, R_0 = 0.831 μm | RMSE = 0.139 μm, R^2 = 0.6269



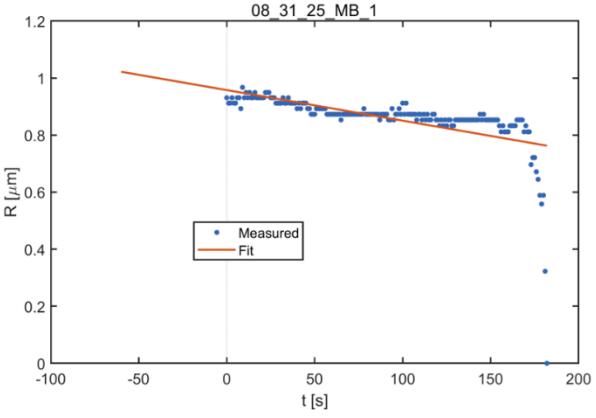
Least Squares Fit | h = 4.23 μm/s, R_0 = 0.723 μm | RMSE = 0.138 μm, R^2 = 0.4767



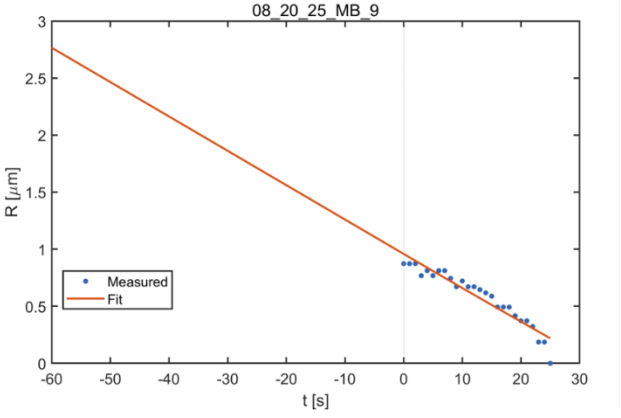
Least Squares Fit | h = 3.96 μm/s, R_0 = 0.866 μm | RMSE = 0.143 μm, R^2 = 0.6564



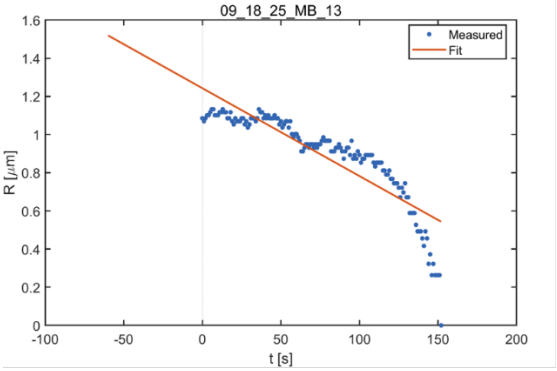
Least Squares Fit | h = 1.37 μm/s, R_0 = 0.666 μm | RMSE = 0.0769 μm, R^2 = 0.3511



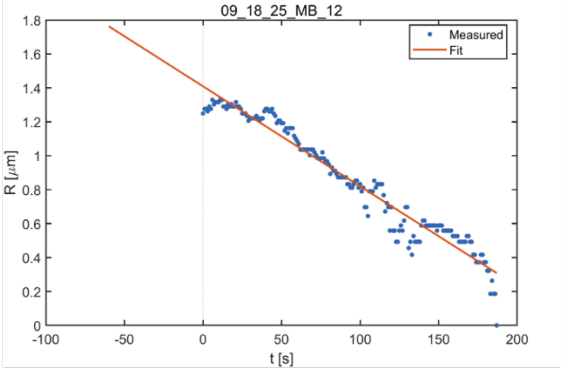
Least Squares Fit | h = 37.3 μm/s, R_0 = 1.3 μm | RMSE = 0.0695 μm, R^2 = 0.9112



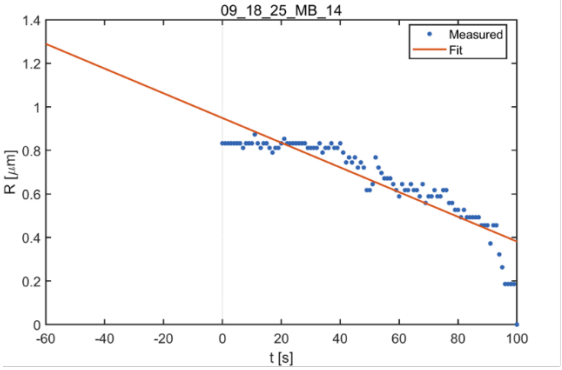
Least Squares Fit | h = 5.89 μm/s, R_0 = 0.897 μm | RMSE = 0.111 μm, R^2 = 0.7718



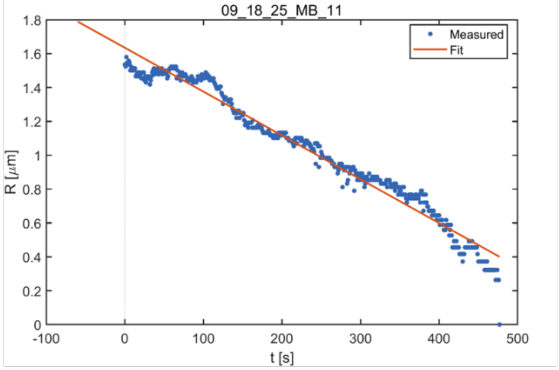
Least Squares Fit | h = 7.53 μm/s, R_0 = 0.999 μm | RMSE = 0.0724 μm, R^2 = 0.9512



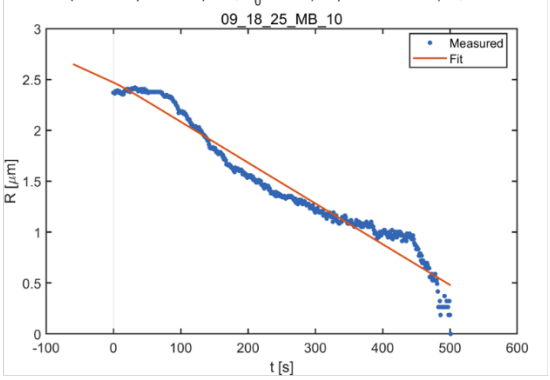
Least Squares Fit | h = 7.26 μm/s, R_0 = 0.791 μm | RMSE = 0.0801 μm, R^2 = 0.8100



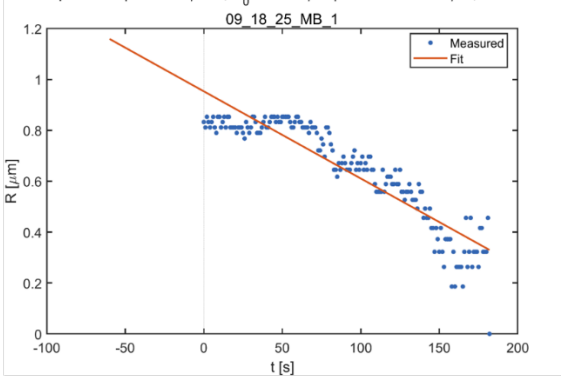
Least Squares Fit | h = 3.32 μm/s, R_0 = 1.02 μm | RMSE = 0.0633 μm, R^2 = 0.9696



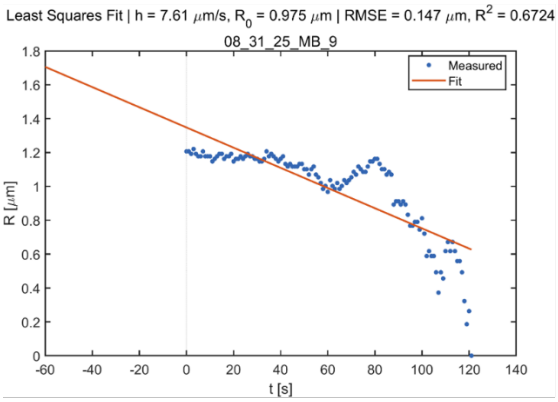
Least Squares Fit | h = 5.12 μm/s, R_0 = 1.38 μm | RMSE = 0.12 μm, R^2 = 0.9590



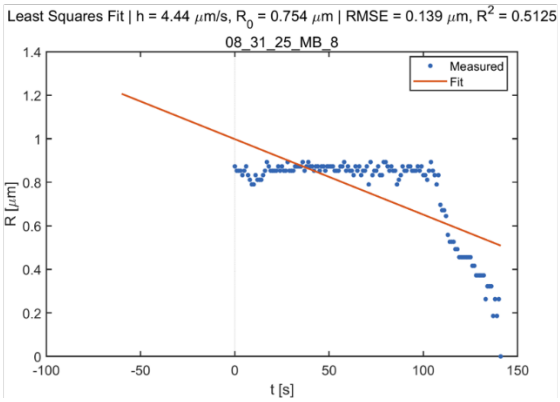
Least Squares Fit | h = 4.39 μm/s, R_0 = 0.732 μm | RMSE = 0.0796 μm, R^2 = 0.8378

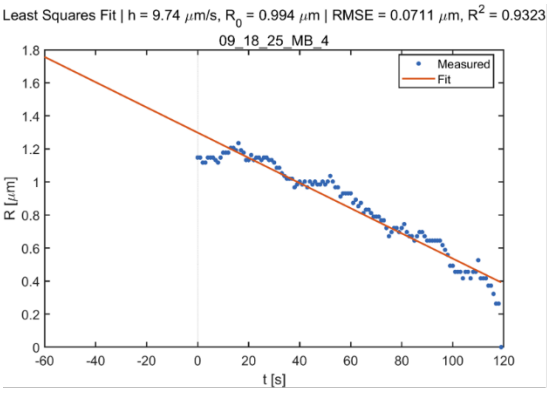


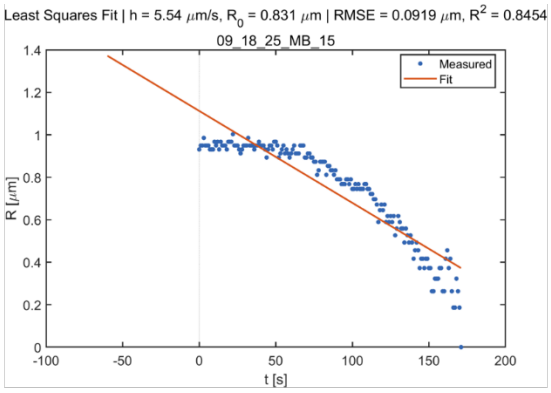
Least Squares Fit | h = 7.61 μm/s, R_0 = 0.975 μm | RMSE = 0.147 μm, R^2 = 0.6724

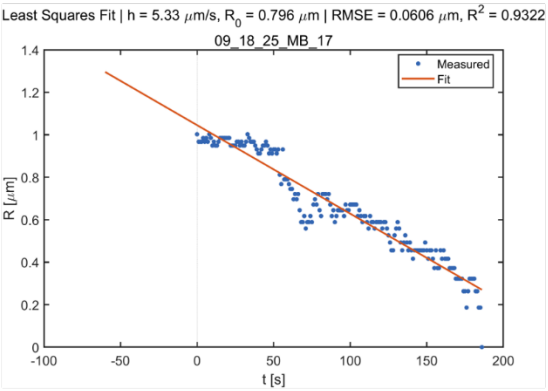


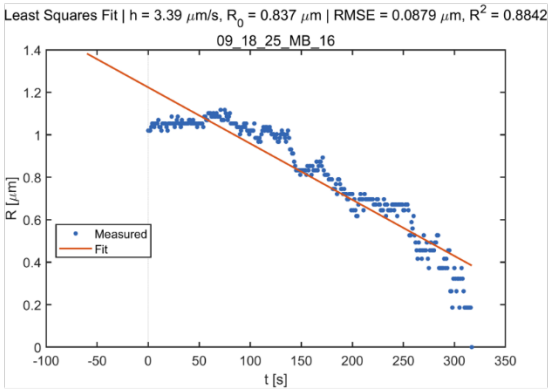
Least Squares Fit | h = 4.44 μm/s, R_0 = 0.754 μm | RMSE = 0.139 μm, R^2 = 0.5125

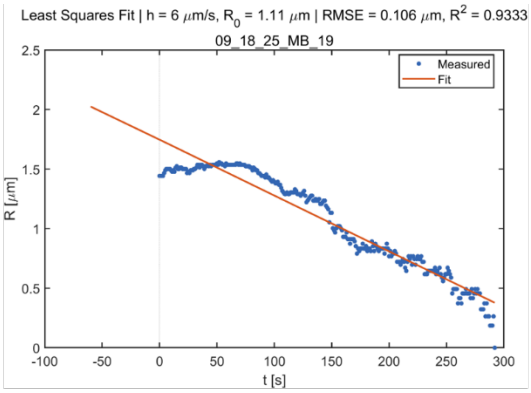


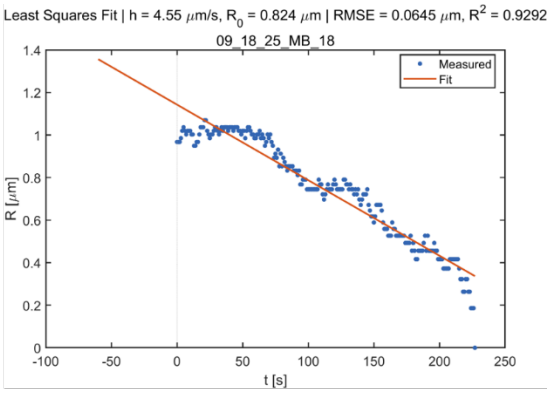

Least Squares Fit | h = 9.74 μm/s, R0 = 0.994 μm | RMSE = 0.0711 μm, R2 = 0.9323
09_18_25_MB_4
Measured
Fit
R [μm]
t [s]

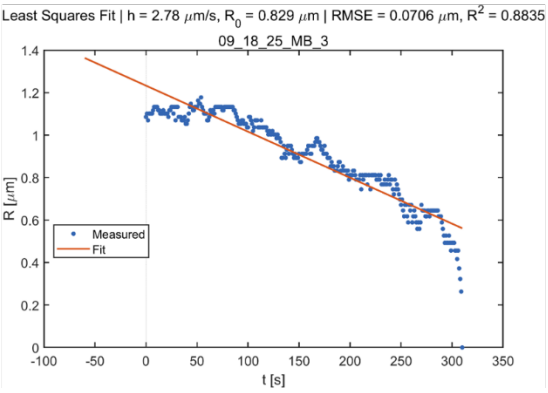

Least Squares Fit | h = 5.54 μm/s, R0 = 0.831 μm | RMSE = 0.0919 μm, R2 = 0.8454
09_18_25_MB_15
Measured
Fit
R [μm]
t [s]

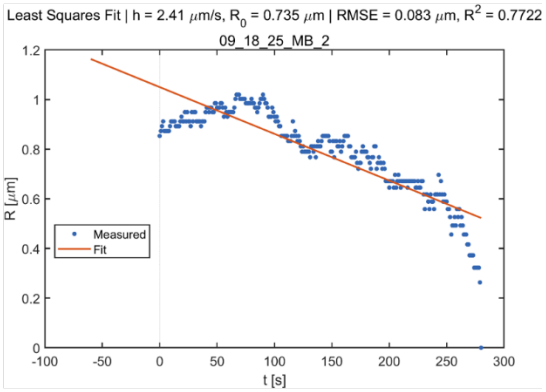

Least Squares Fit | h = 5.33 μm/s, R0 = 0.796 μm | RMSE = 0.0606 μm, R2 = 0.9322
09_18_25_MB_17
Measured
Fit
R [μm]
t [s]


Least Squares Fit | h = 3.39 μm/s, R0 = 0.837 μm | RMSE = 0.0879 μm, R2 = 0.8842
09_18_25_MB_16
Measured
Fit
R [μm]
t [s]


Least Squares Fit | h = 6 μm/s, R0 = 1.11 μm | RMSE = 0.106 μm, R2 = 0.9333
09_18_25_MB_19
Measured
Fit
R [μm]
t [s]


Least Squares Fit | h = 4.55 μm/s, R0 = 0.824 μm | RMSE = 0.0645 μm, R2 = 0.9292
09_18_25_MB_18
Measured
Fit
R [μm]
t [s]


Least Squares Fit | h = 2.78 μm/s, R0 = 0.829 μm | RMSE = 0.0706 μm, R2 = 0.8835
09_18_25_MB_3
Measured
Fit
R [μm]
t [s]


Least Squares Fit | h = 2.41 μm/s, R0 = 0.735 μm | RMSE = 0.083 μm, R2 = 0.7722
09_18_25_MB_2
Measured
Fit
R [μm]
t [s]

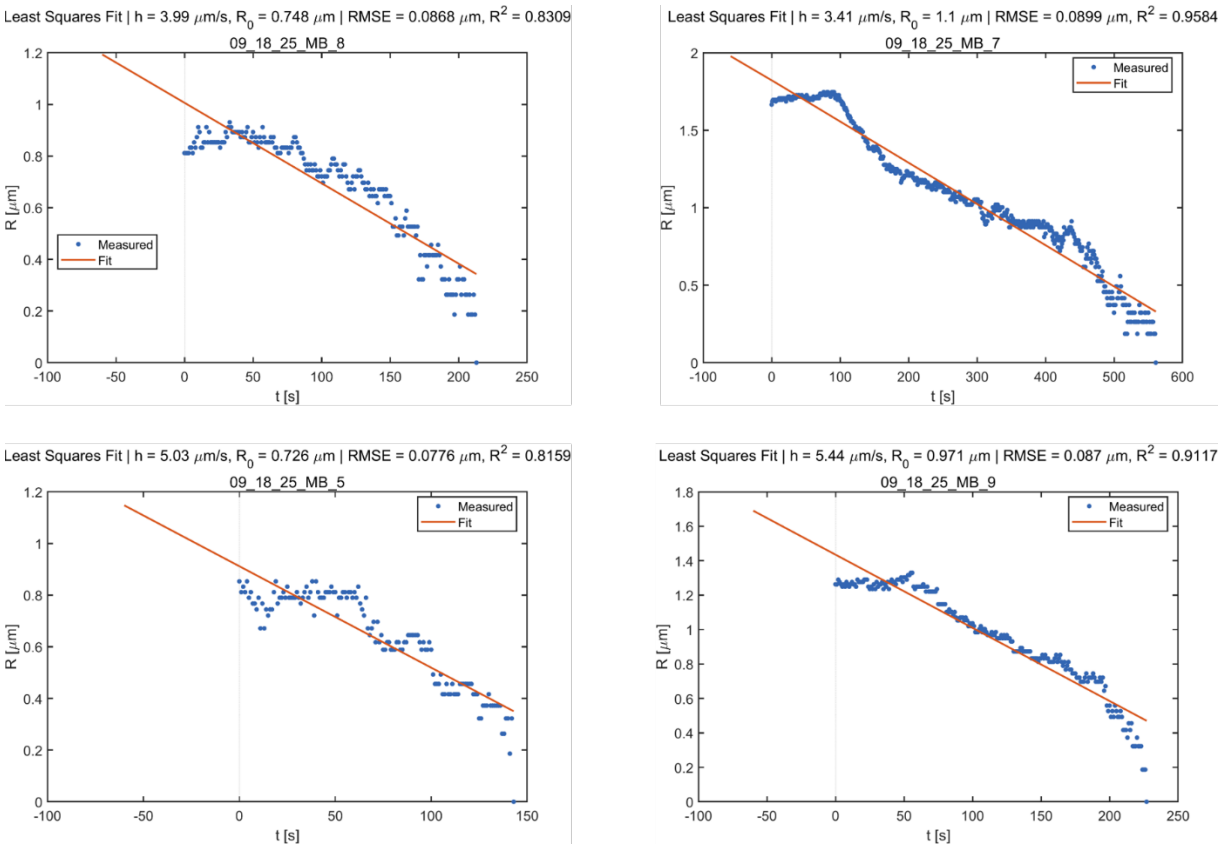


Figure S3. Fitted model on experimental data. Plot of the fitted model (orange; including the 60s prior washing) vs the experimentally measured radius (blue dots). For each curve, h_{C3F8} and R_0 were fitted, and the RMSE and R^2 were computed.

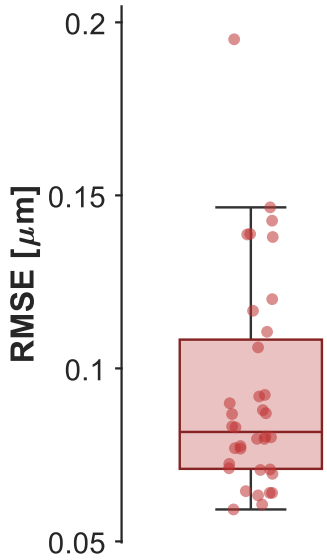


Figure S4. Root Mean Square Error (RMSE) of the final fitted model vs data. Each dot represents the RMSE of the final fitted model versus the data it has been fitted on.

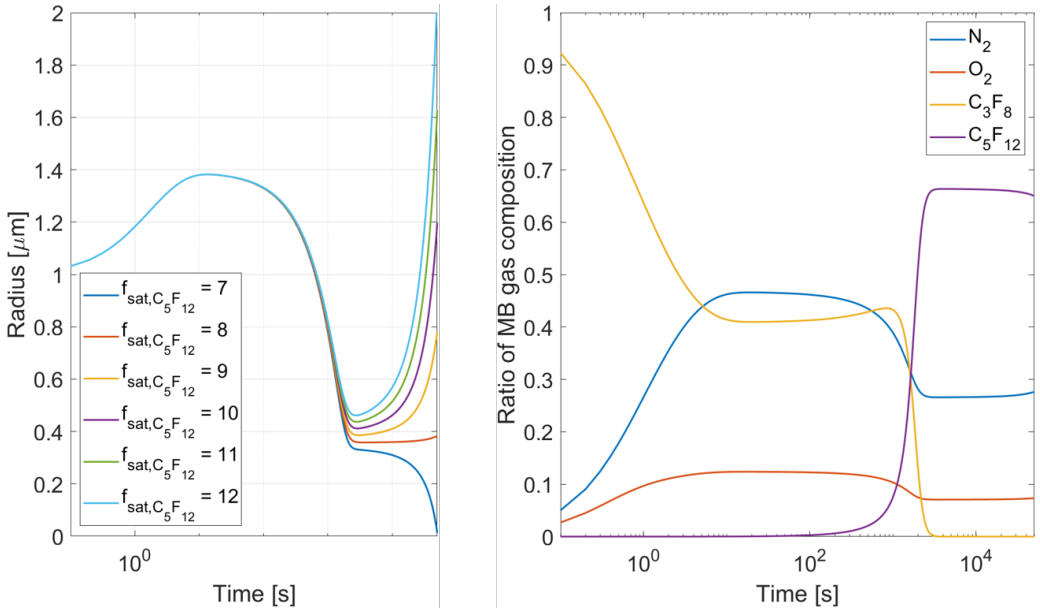


Figure S5. Evolution of MB radius and core gas composition in PFP-supersaturated media. Left: MB radii over time given different PFP supersaturation level. Right: MB core gas composition over time with $f_{sat,C5F12}$ = 8.

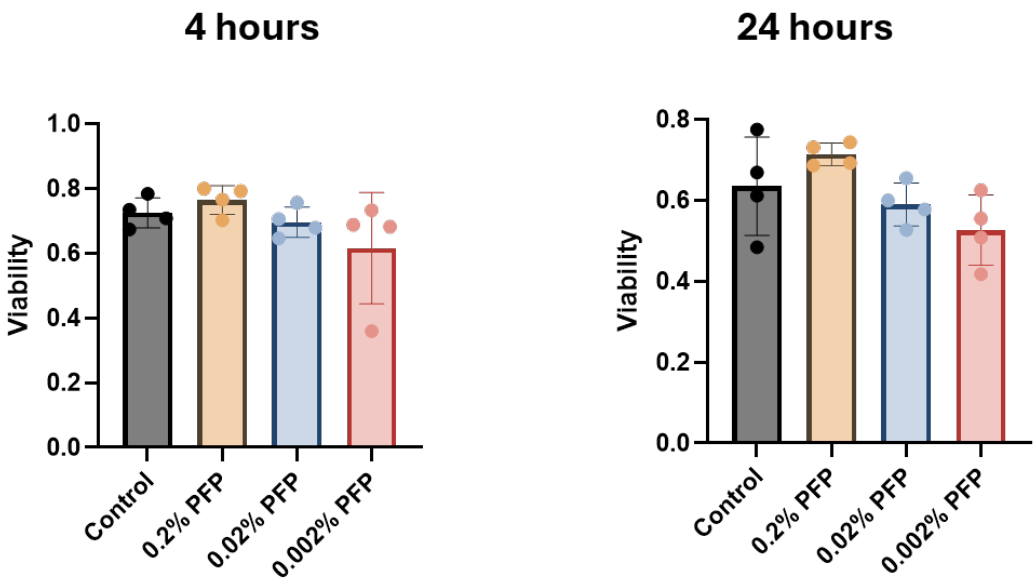


Figure S6. BMDMs viability 6- and 24-hour post co-incubation with PFP-saturated media (0.2%, 0.02%, 0.002%). Left: 6 hours after the co-incubation; Right: 24 hours after the co-incubation, n=4 wells for all conditions. No significant differences were observed between the control and the rest of the groups. Data are presented as mean values +/- SD. P values were determined by one-way ANOVA followed by Dunnett correction for multiple comparisons (control vs. groups).

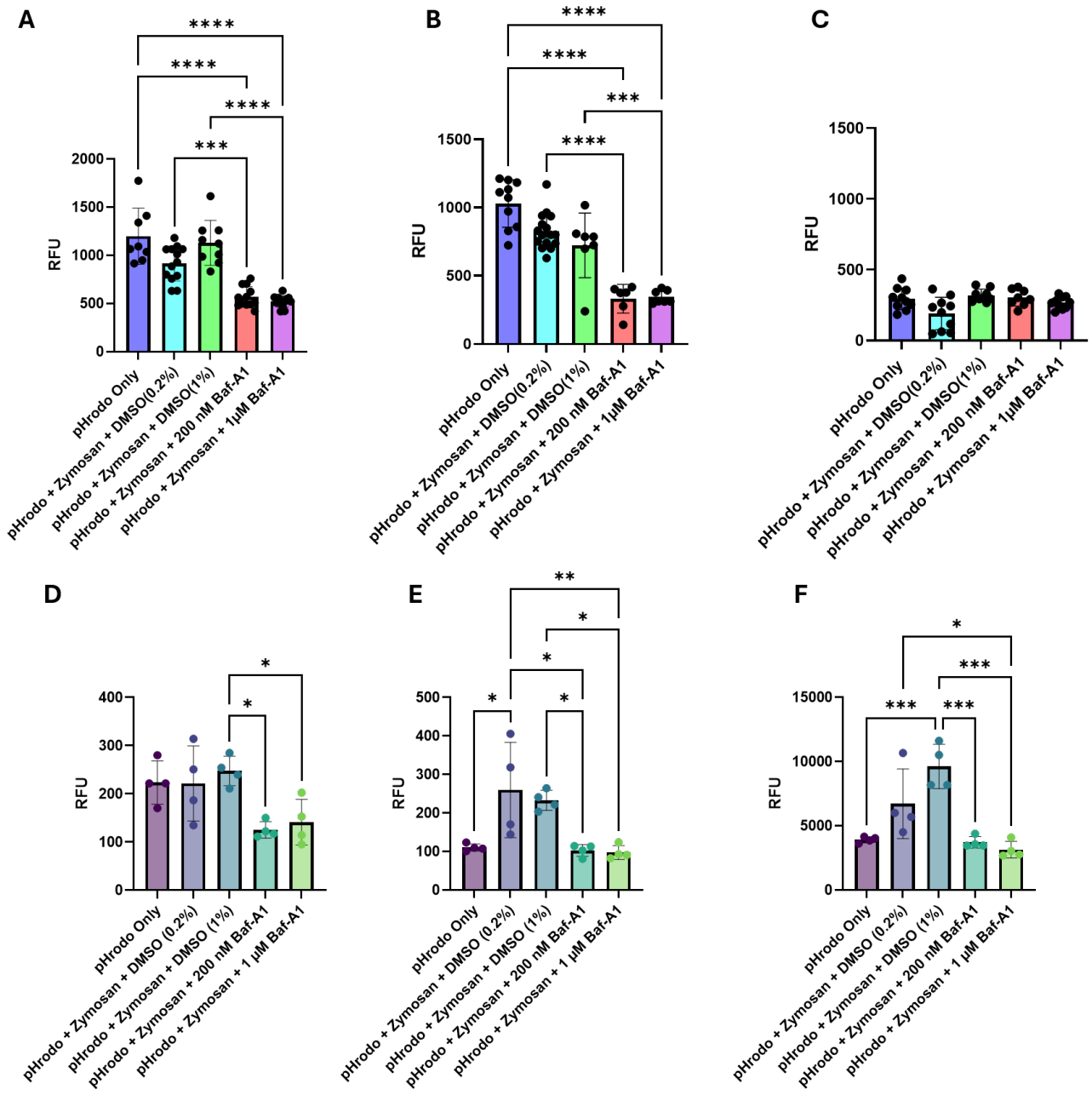


Figure S7. Confirmation of RAW 264.7 and BMDMs enzymatic inhibition with Baf-A1 via pHrodo fluorescence macroscopic imaging. **(A)** 1 hour , **(B)** 3 hours and **(C)** 20 hours RAW 264.7 pHrodo average fluorescence intensity per well (n ≥8 analyzed images across 3 wells) for RAW 264.7 macrophages treated with pHrodo (pH-sensitive fluorescent marker), pHrodo + Zymosan (phagocytic trigger) + DMSO (Baf-A1 vehicle), and pHrodo + Zymosan (phagocytic trigger) + Baf-A1. **(D)** 1 hour , **(E)** 4 hours and **(F)** 24 hours BMDMs pHrodo average fluorescence intensity per well (n = 4 wells) for BMDMs macrophages treated with pHrodo (enzymatic fluorescence marker), pHrodo + Zymosan (phagocytic trigger) + DMSO (Baf-A1 vehicle), and pHrodo + Zymosan (phagocytic trigger) + Baf-A1. Data are presented as mean values +/- SD. P values were

determined by a one-way ANOVA followed by Tukey's correction for multiple comparisons. n.s. - not significant. * $P \leq 0.05$, ** $P \leq 0.01$, *** $P \leq 0.001$

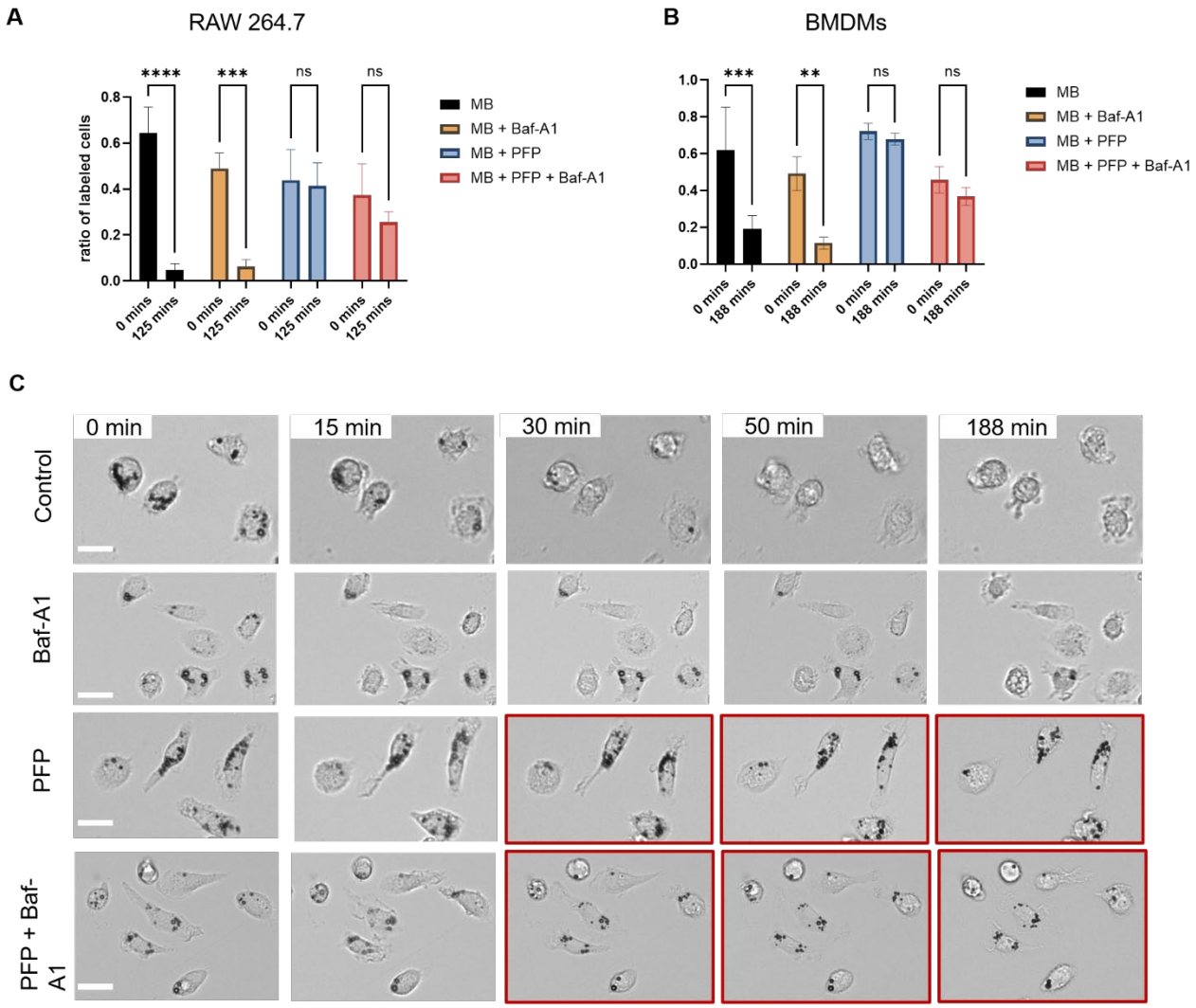


Figure S8. Difference between initial and final time points in ratio of labeled cells among same experiment group. **(A)** RAW 264.7 and **(B)** BMDMs. **(C)** Live microscopy imaging of MB-BMDMs (20x) with 4 different conditions. By row, from top to bottom, MB only (control), MB + Baf-A1 (digestion process stopped), MB + PFP (PFP concentration: 0.002%, compensates for initial diffusion of core gas), MB + Baf-A1 + PFP. Data are presented as mean values +/- SD. P values were determined by a two-way ANOVA followed by Holm-Sidak correction for multiple comparisons. n.s. - not significant. * $P \leq 0.05$, ** $P \leq 0.01$, *** $P \leq 0.001$.

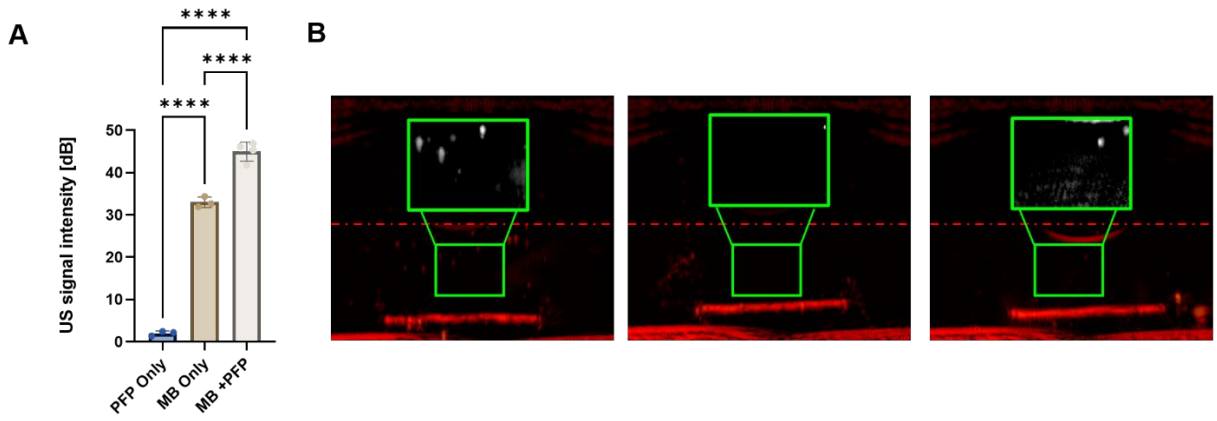


Figure S9. PFP controls alone with ultrasound imaging. (A) Ultrasound signal intensity at time 0 for the following groups: PFP only, MB only, MB+PFP. **(B)** Ultrasound image of the three controls of PFP supersaturated media alone. Data are presented as mean values +/- SD. P values were determined by a one-way ANOVA followed by Tukey's correction for multiple comparisons. n.s. - not significant. ****P ≤ 0.0001

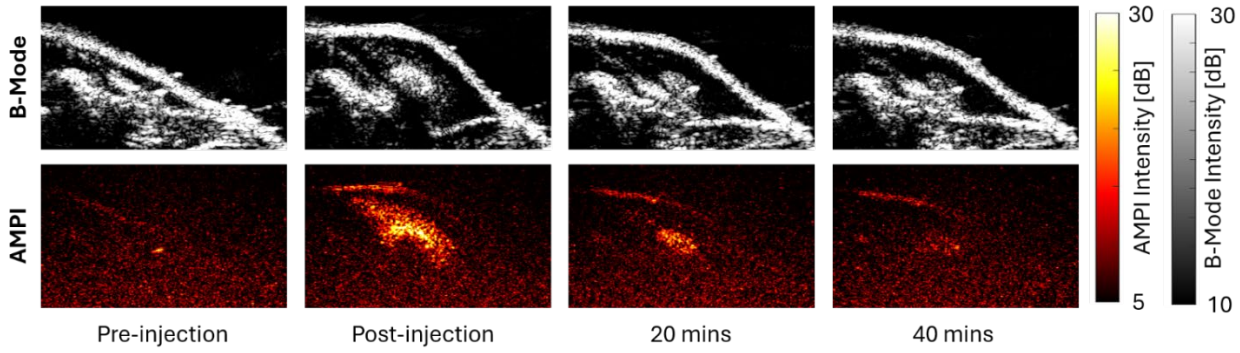


Figure S10. Split AMPI and B-Mode ultrasound imaging of the subcutaneous MB-Mac injection (same dataset as Fig. 6A but not overlaid).

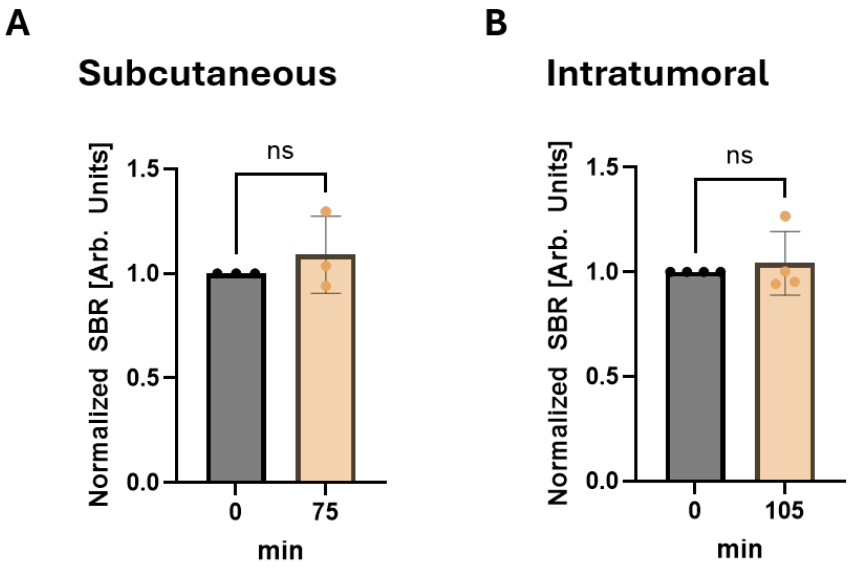


Figure S11. Comparison of AMPI signal in PFP group between initial and final timepoint. **(A)** Statistical comparison between the normalized SBR from the subcutaneously injected PFP group at the initial timepoint (T = 0 min) and final timepoint (T = 75 min). **(B)** Statistical comparison between the normalized SBR from the intratumorally injected PFP group at the initial timepoint (T = 0 min) and final timepoint (T = 105 min). Data are presented as mean values ± SD. p-values were determined by a two-tailed unpaired t-test. n.s. not significant.

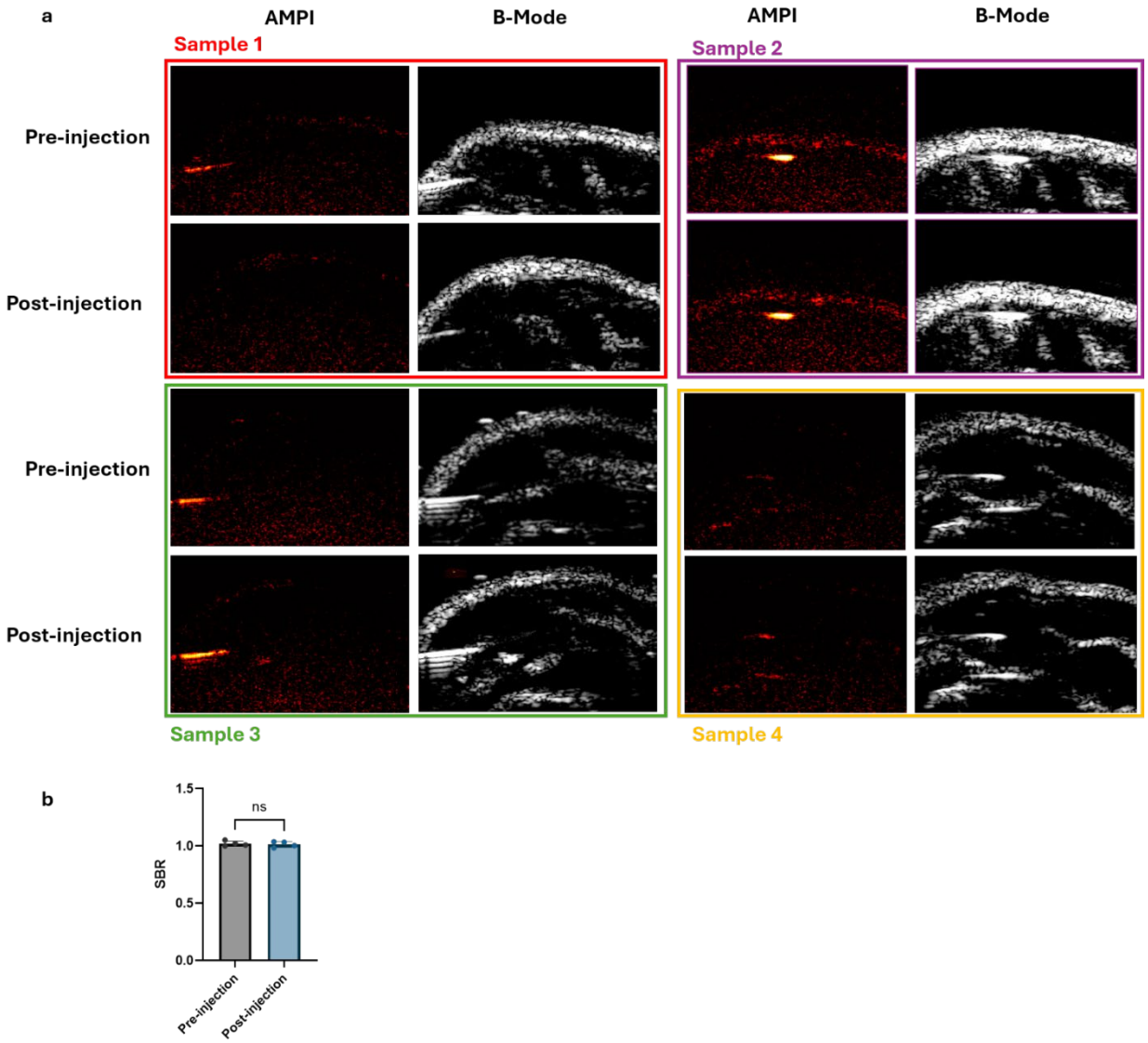


Figure S12. Control imaging with 0.02% PFP-saturated PBS only. (a) Each panel represents an injection of PFP-saturated PBS pre- and post- injection for the 4 samples tried. (b) Statistical comparison between pre- and post- injection SBR. Data are presented as mean values ± SD. p values were determined by a two-tailed unpaired t-test; n.s. not significant.

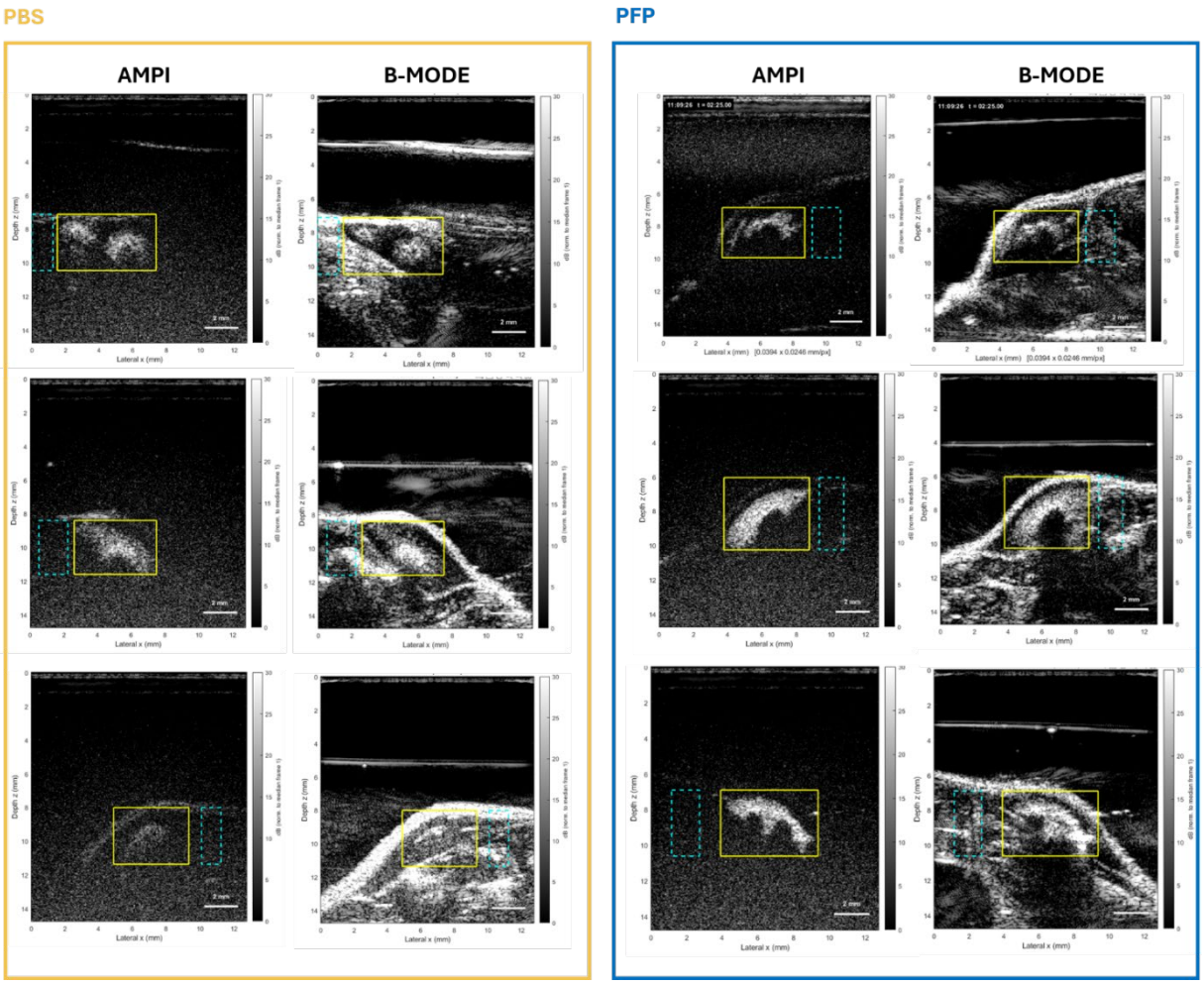


Figure S13. ROI definitions for subcutaneously injected MB-Mac with PBS or PFP. Signal ROI (solid yellow) and depth-matched background ROI (dashed cyan).

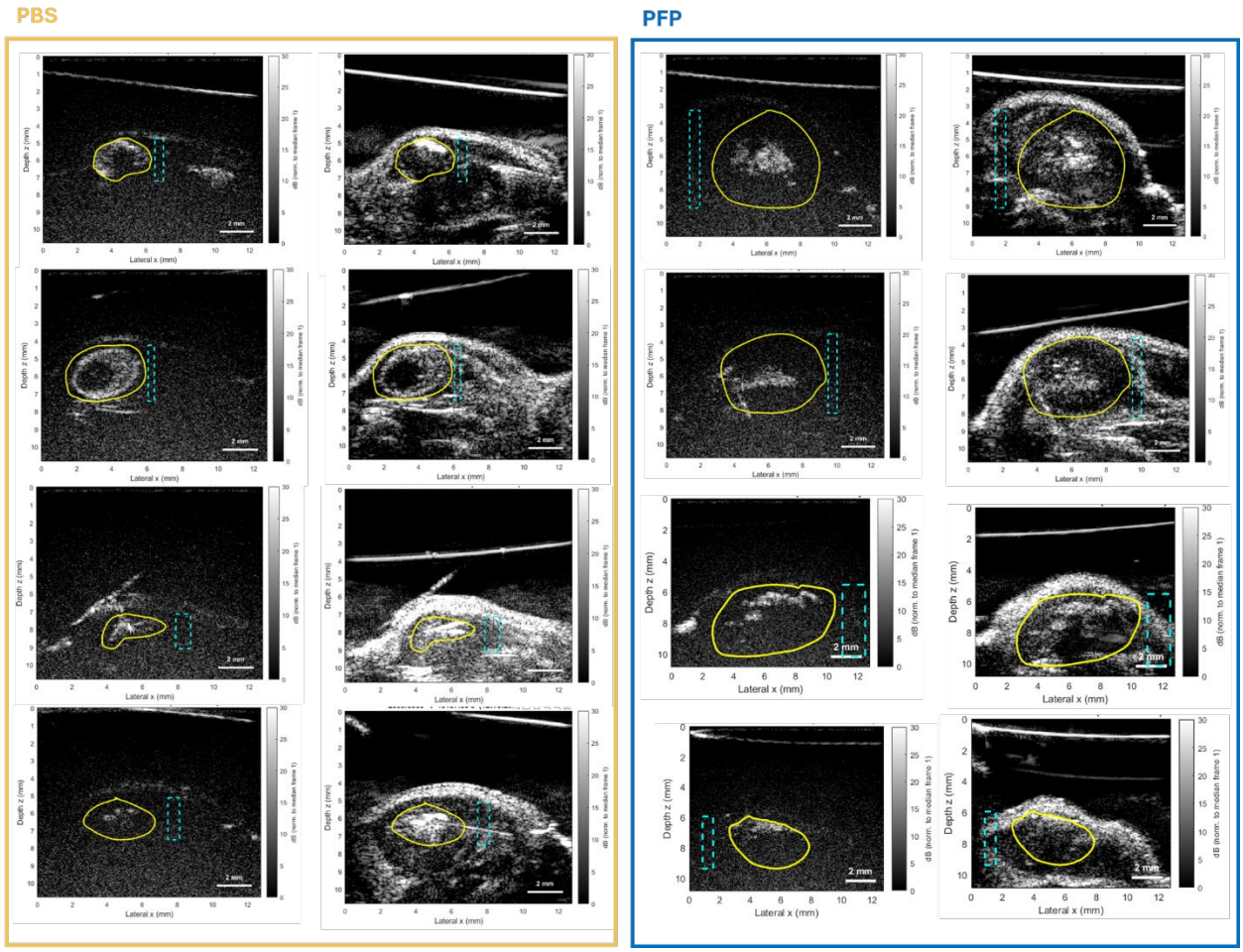


Figure S14. ROI definitions for intratumorally injected MB-Mac with PBS or PFP. Signal ROI (solid yellow) and depth-matched background ROI (dashed cyan).

Table S1. Parameter values used to simulate Figure 2G

Symbol	Description	Value
R_0	Initial bubble radius	1.0×10^{-6} m (1 μm)
Constants and ambient conditions		
T	Absolute temperature of the medium	298.15 K
B	Universal gas constant	8.314462618 J mol^{-1} K^{-1}
σ	Surface tension of the gas–liquid interface (worst case is assumed)	0.025 N m^{-1}
$P_{atm} = P_H$	Ambient (hydrostatic) pressure on the bubble	101 325 Pa (1 atm)
Gas transport properties		
D_{N_2}	Diffusivity of N_2 in water	2.00×10^{-9} m^2 s^{-1}
D_{O_2}	Diffusivity of O_2 in water	2.42×10^{-9} m^2 s^{-1}
$D_{C_3F_8}$	Diffusivity of C_3F_8 in water	7.45×10^{-10} m^2 s^{-1}
K_{H,N_2}	Henry's-law solubility of N_2 in water	6.118×10^{-6} mol m^{-3} Pa^{-1}
K_{H,O_2}	Henry's-law solubility of O_2 in water	1.234×10^{-5} mol m^{-3} Pa^{-1}
K_{H,C_3F_8}	Henry's-law solubility of C_3F_8 in water	2.098×10^{-7} mol m^{-3} Pa^{-1}
h_{N_2}	Shell permeability to N_2	2.857×10^{-5} m s^{-1}
h_{O_2}	Shell permeability to O_2	2.857×10^{-5} m s^{-1}
$h_{C_3F_8}$	Shell permeability to C_3F_8	5.3×10^{-6} m s^{-1}
P_{∞,N_2}	Partial pressure of N_2 in the far-field liquid (0.79 atm)	80 046.75 Pa
P_{∞,O_2}	Partial pressure of O_2 in the far-field liquid (0.21 atm)	21 278.25 Pa
P_{∞,C_3F_8}	Partial pressure of C_3F_8 in the far-field liquid	0 Pa

Table S2. Parameter values used to simulate Figure 3B and 3C, varying the bulk saturation factor of the second fluorocarbon. Gas indices follow the model ordering N_2, O_2, C_3F_8, C_5F_{12}.

Symbol	Description	Value
Driver script / function arguments		
$h_{C_3F_8}$	Shell permeability to C_3F_8	1.0×10^{-6} m s^{-1}
$h_{C_5F_{12}}$	Shell permeability to C_5F_{12}	9.0×10^{-8} m s^{-1}
R_0	Initial bubble radius	1×10^{-6} m (1 μm)
$f_{sat,C_5F_{12}}$	Swept bulk saturation factor of dissolved C_5F_{12}	5,15,25,35
Constants and ambient conditions		
T	Absolute temperature of the medium	298.15 K
B	Universal gas constant	8.314462618 J mol^{-1} K^{-1}
σ	Surface tension of the gas–liquid interface (worst case is assumed)	0.025 N m^{-1}
$P_{atm} = P_H$	Ambient (hydrostatic) pressure on the bubble	101 325 Pa (1 atm)
Gas transport properties		
D_{N_2}	Diffusivity of N_2 in water	2.00×10^{-9} m^2 s^{-1}
D_{O_2}	Diffusivity of O_2 in water	2.42×10^{-9} m^2 s^{-1}
$D_{C_3F_8}$	Diffusivity of C_3F_8 in water	7.45×10^{-10} m^2 s^{-1}
$D_{C_5F_{12}}$	Diffusivity of C_5F_{12} in water	6.30×10^{-10} m^2 s^{-1}
K_{H,N_2}	Henry's-law solubility of N_2 (1.713e-4 / 28)	6.118×10^{-6} mol m^{-3} Pa^{-1}
K_{H,O_2}	Henry's-law solubility of O_2 (3.948e-4 / 32)	1.234×10^{-5} mol m^{-3} Pa^{-1}
K_{H,C_3F_8}	Henry's-law solubility of C_3F_8 (5.2e-4 / BT)	2.098×10^{-7} mol m^{-3} Pa^{-1}
$K_{H,C_5F_{12}}$	Henry's-law solubility of C_5F_{12} (1.17e-4 / BT)	4.720×10^{-8} mol m^{-3} Pa^{-1}
h_{N_2}	Shell permeability to N_2	2.857×10^{-5} m s^{-1}
h_{O_2}	Shell permeability to O_2	2.857×10^{-5} m s^{-1}
$h_{C_3F_8}$	Shell permeability to C_3F_8	1.0×10^{-6} m s^{-1}
$h_{C_5F_{12}}$	Shell permeability to C_5F_{12}	9.0×10^{-8} m s^{-1}